Full length article

# Mechanical behavior and collagen structure of degenerative mitral valve leaflets and a finite element model of primary mitral regurgitation

Mohammad Javad Sadeghinia[a], Hans Martin Aguilera[a], Stig Urheim[c,d],
Robert Matongo Persson[c,d], Vegard Skalstad Ellensen[c], Rune Haaverstad[c,d],
Gerhard A. Holzapfel[a,b], Bjørn Skallerud[a], Victorien Prot[a,*]

[a] Department of Structural Engineering, Norwegian University of Science and Technology, Trondheim, Norway
[b] Institute of Biomechanics, Graz University of Technology, Austria
[c] Haukeland University Hospital, Department of Heart Disease, Bergen, Norway
[d] Institute of Clinical Science, University of Bergen, Bergen, Norway

## ARTICLE INFO

## ABSTRACT

Degenerative mitral valve disease is the main cause of primary mitral regurgitation with two phenotypes: fibroelastic deficiency (FED) often with localized myxomatous degeneration and diffuse myxomatous degeneration or Barlow's disease. Myxomatous degeneration disrupts the microstructure of the mitral valve leaflets, particularly the collagen fibers, which affects the mechanical behavior of the leaflets. The present study uses biaxial mechanical tests and second harmonic generation microscopy to examine the mechanical behavior of Barlow and FED tissue. Three tissue samples were harvested from a FED patient and one sample is from a Barlow patient. Then we use an appropriate constitutive model by excluding the collagen fibers under compression. Finally, we built an FE model based on the echocardiography of patients diagnosed with FED and Barlow and the characterized material model and collagen fiber orientation. The Barlow sample and the FED sample from the most affected segment showed different mechanical behavior and collagen structure compared to the other two FED samples. The FE model showed very good agreement with echocardiography with $2.02 \pm 1.8$ mm and $1.05 \pm 0.79$ mm point-to-mesh distance errors for Barlow and FED patients, respectively. It has also been shown that the exclusion of collagen fibers under compression provides versatility for the material model; it behaves stiff in the belly region, preventing excessive bulging, while it behaves very softly in the commissures to facilitate folding.

**Statement of significance**

This study quantifies for the first time the collagen microstructure and mechanical behavior of degenerative mitral valve (DMV) leaflets. These data will then be used for the first disease-specific finite element (FE) model of DMV. While current surgical repair of DMV is based on surgical experience, FE modeling has the potential to support decision-making and make outcomes predictable. We adopt a constitutive model to exclude collagen fiber under compressions, an important consideration when modeling the mitral valve, where the leaflets are folded to ensure complete closure. The results of this study provide essential data for understanding the relationship between collagen microstructure and degenerative mitral valve mechanics.

## 1. Introduction

Mitral regurgitation (MR) is a common valvular heart disease with frequent complications [1]. The prevalence of MR increases

significantly with age from 6.4% in the 65 − 74 year old to 9.4% in the 75 and older groups [2]. The main cause of primary MR is the degenerative mitral valve (DMV) [2] with two distinct phenotypes; fibroelastic deficiency (FED) and diffuse myxomatous degeneration, also known as Barlow's disease in severe cases. FEDs often involve ruptured chordae with myxomatous degeneration histologically predominant in the posterior leaflet. Diffuse myxomatous degeneration, on the other hand, is a myxomatous degeneration and affects multiple segments of the mitral valve leaflets [3,4]. Myxomatous degeneration is associated with a disrupted microstructure of the mitral valve leaflets [5–7] that alters the mechanical behavior of the leaflets. The altered mechanical behavior alongside the other associated complications with DMV, e.g., abnormal annular dynamics [8], impairs the function of the mitral valve (MV) apparatus.

The numerical simulation can complement the clinical assessment of primary MR, which is mainly based on descriptive evaluations as reported by Zoghbi et al. [9]. However, accurate numerical simulations require accurate material modeling to fully capture the altered state of DMV leaflets compared to a healthy and functional mitral valve. This requires capturing the mechanical behavior, understanding the microstructure change, and using appropriate constitutive modeling.

Very little is known about the mechanical behavior of DMV leaflets. There is only one study on the mechanical properties of DMV leaflets by Barber et al. [10]. The study is based on uniaxial testing without microstructural data insufficient for modeling and it neglects the distinction between FED and diffuse myxomatous degeneration. Therefore, very few studies have performed a numerical simulation of MR due to DMV, all using data from the Barber et al. study [11–14]. Other researchers have investigated the secondary MR assuming similar mechanical properties to healthy MV leaflet tissues [15–19], although it has been shown that the material behavior in the secondary MR differs from healthy MV tissue [20,21].

In addition to the lack of data on mechanical behavior, the collagen distribution in DMV leaflets is unknown. Collagen, which undergoes drastic changes in DMV [5,7], is the main load carrier in mitral valve leaflets [22]. Due to the unknown collagen distribution in the DMV leaflets, simple material models are used in the FE simulation of DMV apparatus, such as isotropic [11], anisotropic with assumed fiber direction and no dispersion [12] or anisotropic with symmetrically high dispersion, i.e., almost isotropic [13,14].

Although there are sophisticated constitutive models for mitral valve leaflets, e.g., [23–25], their potential is limited because of the limited mechanical and microstructural data of DMV leaflets. On the other hand, modern technologies are available today. They have been applied to healthy human or animal tissue to provide detailed microstructural information, such as second harmonic generation (SHG) microscopy [22,25], polarized spatial frequency domain imaging [26,27], electron microscopy [28], and small-angle X-ray or light scattering [29–31]. Collagen distribution is particularly important in modeling, as collagen fibers sustain hardly any compressive stress and should be excluded, especially in mitral valve leaflets, which are folded during systole to ensure complete closure. To the authors' knowledge, there is no study on primary or secondary MR modeling that excluded the collagen fibers.

In this paper, we characterize the collagen microstructure and mechanical properties of DMV samples. Then we provide the first numerical simulations of MR due to DMV based on accurate material modeling of DMV leaflets. First, the mechanical behavior and collagen distribution of mitral valve leaflets are investigated in two patients, one diagnosed with FED and the other with Barlow. We used a custom-built planar biaxial machine and SHG imaging. Then an appropriate constitutive model that can exclude fibers under compression is adapted to characterize the mechanical behavior

of DMV leaflets. Finally, in ABAQUS [32], numerical simulations are created based on 3D echocardiographic data from a FED and a Barlow patient. As boundary conditions for the model, the pathological motion of the annulus and the papillary muscles are also extracted from 3D echocardiographic data. At the end, the predicted motion of the leaflets is compared with the echocardiography and validated.

## 2. Materials and methods

### 2.1. Tissue acquisition and storage

Tissue samples are harvested peroperatively from one patient diagnosed with FED (female, 60 years, height: 172 cm, weight: 74 kg) and another patient diagnosed with Barlow's disease (male, 49 years, height: 179 cm, weight: 88 kg). Both patients underwent MV repair—tissue resection, chordae transposition and insertion of neochordae, followed by annuloplasty. Three tissue samples were harvested from the FED patient, one sample from the anterolateral commissure (ALC) and two samples from segments A2 and P2, respectively (see Fig. 1). For the Barlow patient, only one sample was collected from the P2 segment. At explantation, the anatomical directions are identified and documented by the surgeon. The samples are then snap frozen and stored in Bergen cardiovascular biobank with identifier 2014/828. Prior to testing, samples are transported to the testing facility in liquid nitrogen by a dry shipper (Worthington CX100, US). The samples are stored in the dry shipper at room temperature until thawed in preparation for mechanical testing. Previous studies, e.g., the study by Salinas et al. [33], showed no mechanical effects on the right atrioventricular valve from the freezing process. After thawing, the anatomical directions are identified and a rectangular section dissected for testing.

This study was approved by the Regional Ethical Committee of West Norway with identifier 2016/2073 and all procedures followed national and EU ethics regulations.

### 2.2. Planar biaxial mechanical test of the DMV leaflets

Mechanical testing is performed using a custom-built planar biaxial testing machine, shown in the previous studies [22,34]. The method was previously published using porcine mitral valves [22]. Briefly, the sample is thawed at room temperature and the thickness is measured photogrammetrically. Then the sample is attached to four hooks on each side marked with four fiducial markers in the center, enclosing an approximate area of 1.5 mm × 1 mm. The size of the samples with an effective test area of $10.3 \pm 0.6$ mm × $6.6 \pm 1.3$ mm, is determined by the dissection performed during surgery, but the fiducial markers are spaced to minimize edge effects in the region of interest. The hooks are connected to the handle mechanism, which can rotate freely. This mechanism allows for self-alignment during sample mounting and
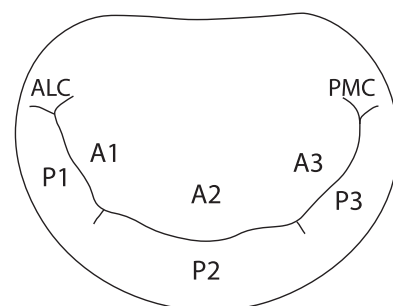


**Fig. 1.** Mitral valve leaflets and its anatomical segments.

minimizes shear forces during the experiments. Before starting the test, a preconditioning of 5 load-unload cycles at a rate of 0.1 mm/s is applied to the maximum load of $1 \pm 0.2$ N. Preconditioning ensures that the sample reaches a stable state, behaves consistently to the test loads, and simulates real-life loading conditions. Unfortunately, a higher maximum load was not feasible due to the sensitivity of the diseased tissue. The sample is also subjected to a preload of 0.01 N in both directions to remove any tissue slack. Three displacement-controlled tests are carried out at a speed of 0.1 mm/s, to the same maximum load of preconditioning. The position of the fiducial markers is tracked and synchronized with the measured forces. Throughout the test, the sample is immersed in a $1 \times$PBS solution at 37°C.

## 2.3. Chemical fixation and clearing of the DMV leaflets

Within 2 hours after thawing and planar biaxial mechanical testing, the same sample is immersed in a 4% formaldehyde solution for chemical fixation. Fixation prevents tissue degradation and preserves the collagen fiber structure. After 18 hours fixation, the FED samples are cleared using 1:2 benzyl alcohol:benzyl benzoate (BABB) [35] and the Barlow sample is cleared using SeeDBp [36]. The BABB protocol was described in detail by Sadeghinia et al. [22]. SeeDBp clearing is based on graded fructose solutions and its main advantage is that it preserves the morphology—it avoids the shrinkage observed in most clearing techniques [37]. The sample is incubated at 25°C in 20 %, 40 %, and 60 % w:v[1] fructose:$0.1 \times$PBS solution each for 4 hours. Then 12 hours in 80 % w:v fructose:$0.1 \times$PBS solution and another 12 hours in 100 % w:v fructose:distilled water solution. Finally, the sample is incubated in the fully saturated fructose solution at 25°C, 80.2 % w:w[2] fructose:distilled water solution for 24 hours. During the incubation process, the solution is rotated at 4 rpm using a tube rotator (PTR-35 Grant Instruments, UK). As shown in Fig. 2, SeeDB exhibits minimal change in tissue morphology and achieves excellent transparency.
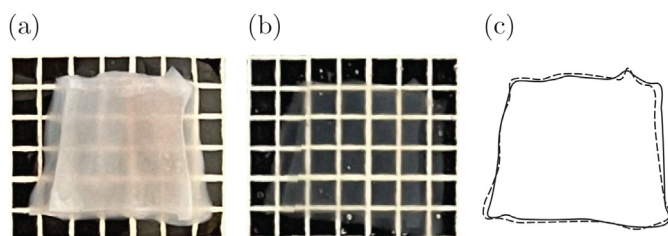


**Fig. 2.** Tissue clearing with SeeDB: (a) fresh porcine heart valve tissue with a thickness of 1 mm immersed in $1 \times$PBS solution; (b) the same tissue after chemical fixation and clearing with SeeDB. Each square is 1 mm × 1 mm; (c) the deformed morphology after clearing (solid curve) compared to the initial morphology (dashed curve). The deformed contour is rotated counter-clockwise by 5° for clarity.

## 2.4. Collagen microstructure of the DMV leaflets

A custom bottom-glass dish is prepared with coverslips and a silicon isolator (Grace Bio-Labs, US). The sample, immersed in a fully saturated fructose solution, is placed in the custom bottom-glass dish and sealed. SHG imaging of collagen fibers is performed with Lecia SP8 (Leica Biosystems, Germany) with laser excitation set at 890 nm. In order to compensate for the scattering at greater depths, the laser power is increased linearly ($z$ compensation). The

Leica HCX IRAPO 25×, NA 0.95 water objective with a working distance of 2.4 mm is used for image acquisition. The forward and backward SHG signals are collected using a standard photomultiplier tube (PMT) and HyD (GaAsP) detectors, respectively. The scanning takes place near the fiducial markers and the coordinates are recorded using a piezoelectric stage (Scan IM 127 × 83, Märzhäuser Wetzlar, Germany) with an accuracy of $\pm 3\,\mu$m. The field of view covers an area of $465\,\mu$m × $465\,\mu$m with a resolution of $0.45\,\mu$m/pixel. Full-thickness imaging is performed at an interval of $5\,\mu$m.

A user-defined MATLAB script based on the method described in our previous study [22] is used to quantify the collagen fiber dispersion for each image. The method uses Fourier transform and wedge filters to construct a probability density function of collagen fiber distributions [38]. The distribution is then fitted by two families of fiber using a von Mises distribution, which is defined as

$$\rho_{\mathrm{vm}}(\theta) = w \frac{1}{\pi} \frac{\exp\{a_1 \cos[2(\theta - \alpha_1)]\}}{I_0(a_1)} + (1 - w)\frac{1}{\pi} \frac{\exp\{a_2 \cos[2(\theta - \alpha_2)]\}}{I_0(a_2)}. \tag{1}$$

Herein $\rho_{\mathrm{vm}}(\theta)$ is the von Mises distribution, characterized by $\alpha$ and $a$, the mean fiber angle and concentration parameter, respectively, and the subscript denotes the first or second fiber family, while $w$ is the weighting factor with values from 0 to 1 and $I_0$ is the zero-order modified Bessel function of the first kind. Figs. 3(a) and (b) show the collagen structure and its corresponding distribution for the Barlow sample at a depth of $200\,\mu$m. The distribution of all images can be stacked to generate a contour map as shown in Fig. 3(c). To improve the signal-to-noise ratio (SNR), the forward and backward SHG signals are combined for the thick Barlow sample. In principle, the collagen fibers are so-called 'forward scattering'—emit more forward SHG signals shown by, e.g., Légaré et al. [39]. However, in thick tissues and layers closer to the objective, the forward signals are more scattered, resulting in a lower SNR. On the other hand, the use of HyD detectors with high sensitivity improves the backward SHG signals, especially in layers close to the objective.

Fig. 4 shows that backward SHG signals provide more detail and contrast in layers near the objective, while forward signals provide more detail at greater depths. Nonetheless, each signal is sufficient to be analyzed independently based on the Fourier transform. In this study we processed the signals from each detector separately and averaged them at the end. The contour plot of the forward signal, shown in Fig. 5(a), provides more detail in layers that penetrate deeper into the tissue. On the other hand, the contour plot of the backward signal, shown in Fig. 5(b), provides more detail in layers closer to the objective. Therefore, we use both signals to create an averaged contour map shown in Fig. 5(c). In addition, the thick Barlow sample is imaged on both sides due to the limited working distance of the objective. To ensure that the image corresponds to the same location from both sides, the fiducial markers are used as reference points – the acquisition site coordinates are recorded with using the piezoelectric stage with an accuracy of $\pm 3\,\mu$m in relation to the fiducial markers. In addition, the image is recorded according to the measured thickness with an overlap of $100\,\mu$m. In Fig. 6, the SHG image from the ventricular side (a) and atrium side (b) is combined to create the entire thickness contour plot (c).

Finally, a representative collagen fiber distribution is defined by averaging and normalizing all the layers of the contour plot. The representative layer is then fitted by the von Mises distribution, eq. (1). The estimated parameters are then used for mechanical parameter estimation and finite element (FE) analysis.

---

[1] w:v is weight-to-volume ratio. It is defined as the ratio of weight in grams of solute to milliliters of solute

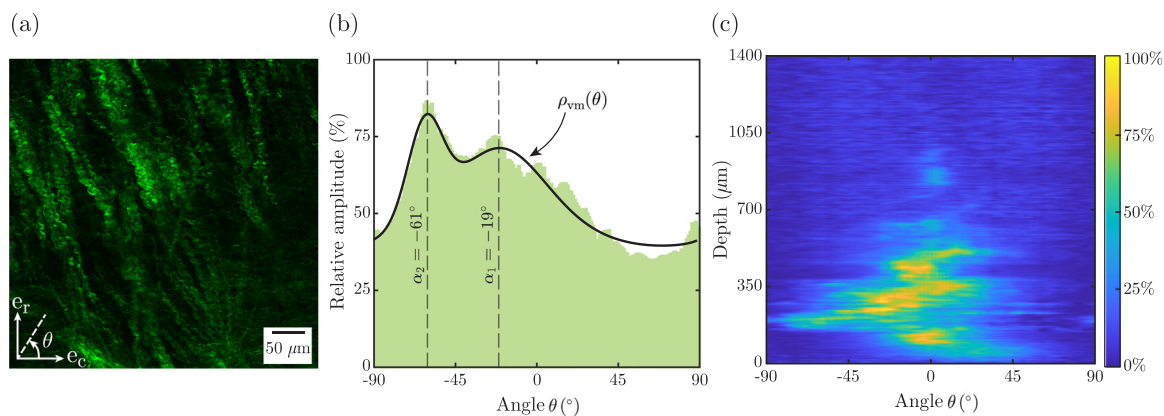[2] w:w is the weight-to-weight ratio

**Fig. 3.** SHG image acquisition and quantified collagen fiber distribution: (a) forward SHG image of the Barlow sample at a depth of $200\,\mu$m from the ventricular side (green = collagen, $r$ = radial, $c$ = circumferential direction); (b) corresponding quantified collagen fiber distribution (green area) based on Fourier transform. The von Mises parameters (solid curve) are $\alpha_1 = -19°$, $a_1 = 1.2$ and $\alpha_2 = -61°$, $a_2 = 10.99$ and $w = 0.82$, with $r^2 = 0.95$; (c) contour plot visualizing the collagen fiber distribution through the thickness based on depth and angle. The color in the contour plot in (c) represents the relative amplitude in (b).. (For interpretation of the references to colour in this figure legend, the reader is referred to the web version of this article.)



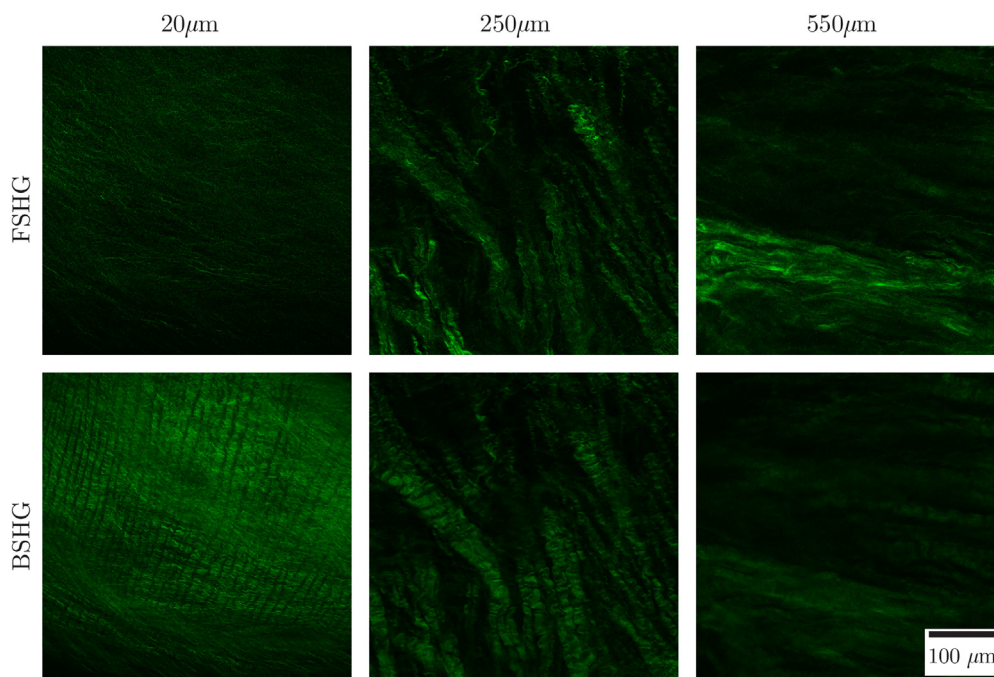**Fig. 4.** Comparison of forward (FSHG) and backward (BSHG) SHG images at depths of $20\,\mu$m, $250\,\mu$m and $550\,\mu$m. The images are from the Barlow sample, which covers an area of $465\,\mu$m $\times$ $465\,\mu$m.
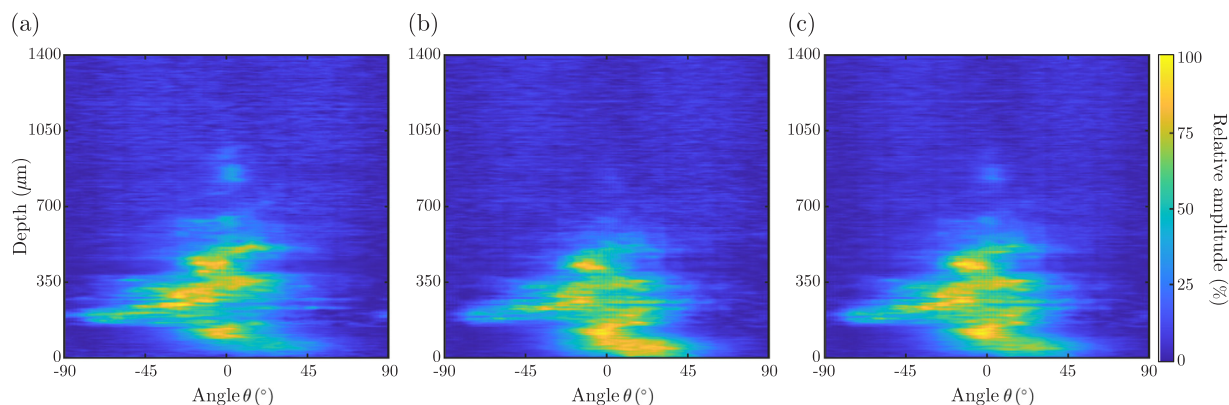


**Fig. 5.** Using forward (a) and backward (b) SHG signals to facilitate in-depth imaging for the thick Barlow sample. The final contour (c) is used for simulation.
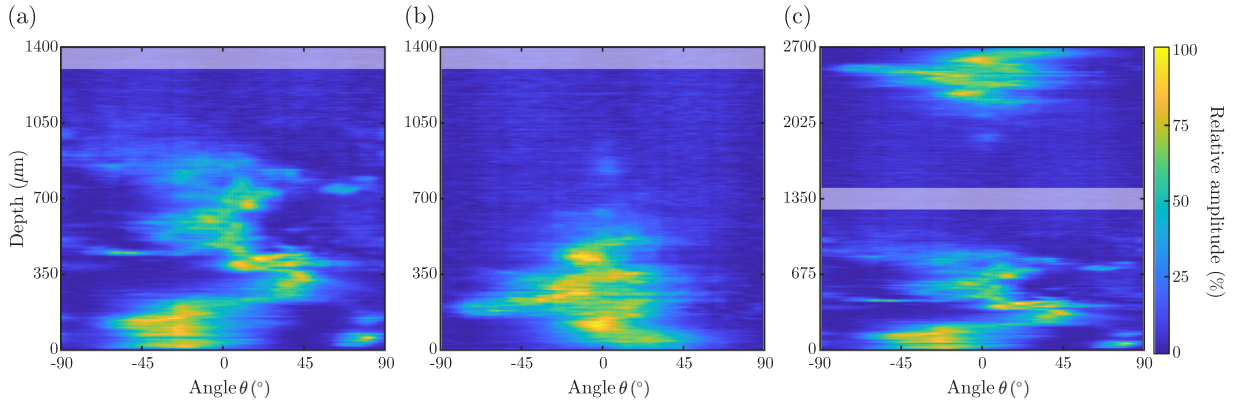
**Fig. 6.** SHG image acquisition from two sides (a) and (b) for the thick Barlow sample to create the entire thickness contour plot (c). The highlighted rectangle shows the 100 $\mu$m overlap according to the previously measured thickness.

## 2.5. Constitutive model for the DMV leaflets

Given the low thickness-to-area ratio of DMV leaflets, the leaflets are modeled assuming a planar dispersion of collagen fibers. The deformation gradient $\mathbf{F}$ is defined in relation to an undeformed reference configuration that is assumed to be stress free. The right Cauchy–Green tensor is then calculated as $\mathbf{C} = \mathbf{F}^{\mathrm{T}}\mathbf{F}$. We assume a hyperelastic material in which the strain-energy function $\Psi$ is decoupled into an isotropic part $\Psi_{\mathrm{iso}}$ and a fiber part $\Psi_{\mathrm{fib}}$. The isotropic function is assumed to be a neoHookean model, i.e.

$$\Psi_{\mathrm{iso}} = \mu(I_1 - 3), \qquad I_1 = \mathrm{tr}\mathbf{C}, \tag{2}$$

where $\mu$ is a positive material parameter and $I_1$ is the first invariant of $\mathbf{C}$, where $\mathrm{tr}(\bullet)$ denotes the trace of $(\bullet)$.

For the fibrous part of the constitutive model, it is of interest to exclude collagen fibers under compression, particularly for the mitral valve apparatus. For the fibrous part $\Psi_{\mathrm{fib}}$ an integration scheme can be formulated with a Heaviside function $\mathcal{H}$ [40] that reads

$$\Psi_{\mathrm{fib}} = \int_{-\frac{\pi}{2}}^{\frac{\pi}{2}} \rho_{\mathrm{vm}}(\theta)\mathcal{H}\psi_{\mathrm{f}}(I_4)\mathrm{d}\theta, \qquad \mathcal{H} = \begin{cases} 1, & I_4 \geq 1, \\ 0, & I_4 < 1, \end{cases} \tag{3}$$

where $\psi_{\mathrm{f}}(I_4)$ is the single fiber strain-energy function for fiber direction $\mathbf{N} = \cos\theta\,\mathbf{e}_{\mathrm{c}} + \sin\theta\,\mathbf{e}_{\mathrm{r}}$, where $\mathbf{e}_{\mathrm{c}}$ and $\mathbf{e}_{\mathrm{r}}$ denote the basis vectors in the circumferential and radial directions, respectively, see Fig. 3(a). Note that because of symmetry, $-\pi/2 \leq \theta < \pi/2$, while $I_4$ is the square of the fiber stretch, defined as $I_4 = \mathbf{C} : \mathbf{N} \otimes \mathbf{N}$, and $\rho_{\mathrm{vm}}(\theta)$ is the probability density function of collagen fiber orientation, see Fig. 3(b). This way $\Psi_{\mathrm{fib}}$ will be equal to zero in the subdomain where $I_4 < 1$. The computational cost of integration and the possibility of a discontinuous function due to the exclusion of compressed fibers are the main disadvantages of the integration scheme. An alternative, proposed by Li et al. [41], is the use of a discretized fiber dispersion. The underlying idea is to assume representative fiber directions over the entire integration domain. Therefore, the integration will be approximated by

$$\Psi_{\mathrm{fib}} \approx \sum_{n=1}^{m} \rho_n \psi_{\mathrm{f}}(I_{4n}), \quad I_{4n} = \mathbf{C} : \mathbf{N}_n \otimes \mathbf{N}_n, \tag{4}$$

where $m$ is the number of representative fibers and $\mathbf{N}_n$ is the $n$th representative fiber, defined as $\mathbf{N}_n = \cos\theta_n\,\mathbf{e}_{\mathrm{c}} + \sin\theta_n\,\mathbf{e}_{\mathrm{r}}$, with $\theta_n = \frac{n-1}{m}\pi - \frac{\pi}{2}$. Also, $\rho_n$ is the corresponding probability density function for the $n$th representative fiber. It is found by

$$\rho_n = \int_{\theta_n}^{\theta_{n+1}} \rho_{\mathrm{vm}}(\theta)\mathrm{d}\theta, \tag{5}$$

where $\rho_{\mathrm{vm}}(\theta)$ is given by eq. (1), which is normalized so that

$$\int_{-\frac{\pi}{2}}^{\frac{\pi}{2}} \rho_{\mathrm{vm}}(\theta)\mathrm{d}\theta = 1 \qquad \text{thus} \sum_{n=1}^{m} \rho_n = 1. \tag{6}$$

To exclude collagen fibers under compression, $\psi_{\mathrm{f}}(I_{4\mathrm{n}})$ is assumed to be zero at $I_{4\mathrm{n}} < 1$. For $I_{4\mathrm{n}} \geq 1$, $\psi_{\mathrm{f}}(I_{4\mathrm{n}})$ can have any permissible form and here the exponential form proposed by Holzapfel et al. [42] is assumed, i.e.

$$\psi_{\mathrm{f}}(I_{4\mathrm{n}}) = \frac{k_1}{2k_2}\{\exp[k_2(I_{4\mathrm{n}} - 1)^2] - 1\}, \qquad I_{4\mathrm{n}} \geq 1. \tag{7}$$

If the tissue is assumed to be incompressible the (total) strain-energy function can then be defined as

$$\Psi = \Psi_{\mathrm{iso}} + \Psi_{\mathrm{fib}} + p(J - 1), \quad J = \det\mathbf{F} > 0, \tag{8}$$

where $p$ is a Lagrange multiplier used to enforce incompressibility, and $J$ is the positive volume ratio.

The second Piola-Kirchhoff tensor $\mathbf{S}$ is found by the derivative of the strain-energy function $\Psi$ with respect to the right Cauchy–Green tensor $\mathbf{C}$. Taking into account eqs. (2), (4), (7) and (8) we get [43]

$$\mathbf{S} = 2\frac{\partial\Psi}{\partial\mathbf{C}} = 2\mu\mathbf{I} + 2\sum_{n=1}^{m} \rho_n\psi_{\mathrm{f}}'(I_{4\mathrm{n}})\mathbf{N}_n \otimes \mathbf{N}_n - p\mathbf{C}^{-1}, \tag{9}$$

in which $\mathbf{I}$ is the second-order identity tensor, and

$$\psi_{\mathrm{f}}'(I_{4n}) = \begin{cases} k_1(I_{4n} - 1)\exp[k_2(I_{4n} - 1)^2], & I_{4n} \geq 1, \\ 0, & I_{4n} < 1. \end{cases} \tag{10}$$

The Cauchy tensor stress $\boldsymbol{\sigma}$ can be calculated as $\boldsymbol{\sigma} = \mathbf{F}\mathbf{S}\mathbf{F}^{\mathrm{T}}$ so that

$$\boldsymbol{\sigma} = 2\mu\mathbf{b} + 2\sum_{n=1}^{m} \rho_n\psi_{\mathrm{f}}'(I_{4n})\mathbf{n}_n \otimes \mathbf{n}_n - p\mathbf{I}, \tag{11}$$

where $\mathbf{b} = \mathbf{F}\mathbf{F}^{\mathrm{T}}$ is the left Cauchy–Green tensor, and $\mathbf{n}_n = \mathbf{F}\mathbf{N}$ is the fiber direction in the current configuration.

## 2.6. Mechanical parameter estimation for the DMV leaflets

In this section, we use the planar biaxial test data and the constitutive model to characterize the mechanical behavior of DMV leaflets. We define three orthogonal unit vectors as $\mathbf{e}_{\mathrm{c}}$, $\mathbf{e}_{\mathrm{r}}$ and $\mathbf{e}_{\mathrm{t}}$ denoting the circumferential, radial, and transmural directions, respectively. In this coordinate system, the deformation gradient $\mathbf{F}$ is calculated from the fiducial markers similar to our previous study [22], and the matrix of $\mathbf{C}$ has only diagonal components, namely

the squares of the principal stretches $\lambda_c^2$, $\lambda_r^2$ and $\lambda_t^2$. Because of incompressibility, the principal stretch $\lambda_t$ is equal to $(\lambda_c \lambda_r)^{-1}$. The $I_{4n}$ is then given by

$$I_{4n} = \lambda_c^2 \cos^2 \theta_n + \lambda_r^2 \sin^2 \theta_n. \tag{12}$$

With $\sigma_{tt} = 0$, and Eq. (11) we obtain the Cauchy stress components as

$$\sigma_{cc} = (2\mu + \alpha)\lambda_c^2 - 2\mu(\lambda_c \lambda_r)^{-2},$$
$$\sigma_{rr} = (2\mu + \beta)\lambda_r^2 - 2\mu(\lambda_c \lambda_r)^{-2}, \tag{13}$$

where

$$\alpha = 2 \sum_{n=1}^{m} \rho_n \psi_f'(I_{4n}) \cos^2 \theta_n,$$
$$\beta = 2 \sum_{n=1}^{m} \rho_n \psi_f'(I_{4n}) \sin^2 \theta_n. \tag{14}$$

The stresses $\sigma_{cc}$ and $\sigma_{rr}$ are calculated from first Piola Kirchhoff stresses, which are based on the measured forces, the thickness, and the effective area measured between the hooks. In the planar biaxial tests $I_{4n} \geq 1$, since $\lambda_c^2$ and $\lambda_r^2 \geq 1$. Therefore the summation in Eq. (14) can be replaced by integration. A user-defined MATLAB script is used to estimate parameters $\mu$, $k_1$, $k_2$ with a nonlinear least squares method – trust region reflective algorithm. The same initial value is assumed for all samples, with $\mu = 1.0$ kPa, $k_1 = 2.0$ kPa and $k_2 = 10.0$. The initial value is also altered to check the global minimum.

## 2.7. Numerical implementation and verification of the constitutive model for the DMV leaflets

The constitutive model presented in Section 2.5 was implemented in ABAQUS [32] using the VUMAT subroutine. At the beginning of the analysis, a subroutine is called to calculate the representative fiber directions $\mathbf{N}_n$ and the associated probability density function $\rho_n$. The modified Bessel function of the first kind in the von Mises distribution, eq. (1), is calculated as

$$I_0(a) = \sum_{j=0}^{\infty} \frac{(\frac{a}{2})^{2j}}{j!^2}. \tag{15}$$

The series was implemented with the first twenty terms in VUMAT. The calculated probability density function $\rho_{vm}$ and the representative direction $\mathbf{N}_n$ are stored in a globally allocatable array[3].

To verify the ABAQUS implementation, single element analyses are performed for simple shear and uniaxial extension. For the simple shear test, the square of the $n$th representative fiber stretch is

$$I_{4n} = c^2 \sin^2 \theta_n + c \sin 2\theta_n + 1, \tag{16}$$

where $c$ is the amount of shear. Then, $I_{4n} \geq 1$ when

$$-\frac{\pi}{2} \leq \theta_n \leq \theta_f = -\arctan(2/c) \text{ and } 0 \leq \theta_n < \frac{\pi}{2}. \tag{17}$$

So, based on the integral, Eq. (3), and the discretized scheme, Eq. (4), the Cauchy stresses are

$$\sigma_{cr} = 2\mu c + 2 \int_{-\frac{\pi}{2}}^{\frac{\pi}{2}} \rho_{vm}(\theta) \psi_f'(\cos\theta + c\sin\theta)\sin\theta d\theta,$$
$$\sigma_{cr} = 2\mu c + 2 \sum_{n=0}^{m} \rho_n \psi_f'(\cos\theta_n + c\sin\theta_n)\sin\theta_n. \tag{18}$$

The uniaxial extension test is a special case of the planar biaxial tests as derived in Section 2.6. For this reason

$$I_{4n} = \lambda_c^2 \cos^2 \theta_n + \lambda_r^2 \sin^2 \theta_n, \tag{19}$$

so $I_{4n} \geq 1$ when

$$-\theta_f \leq \theta_n \leq \theta_f = \arccos\sqrt{\frac{1 - \lambda_r^2}{\lambda_c^2 - \lambda_r^2}}. \tag{20}$$

Note that in a planar fiber distribution, $\lambda_r \neq \lambda_t$. Therefore, the stretch $\lambda_r$ can be computed numerically by solving for $\sigma_{rr}(\lambda_r) = 0$, e.g., by using Newton-Raphson method. Finally, the Cauchy stresses based on the integral, Eq. (3), and the discretized scheme, Eq. (4), are

$$\sigma_{cc} = 2\mu\lambda_1^2 - 2\mu(\lambda_1 \lambda_2)^{-2} + 2\lambda_1^2 \int_{-\frac{\pi}{2}}^{\frac{\pi}{2}} \rho_{vm}(\theta) \psi_f' \cos^2\theta d\theta,$$
$$\sigma_{cc} = 2\mu\lambda_1^2 - 2\mu(\lambda_1 \lambda_2)^{-2} + 2\lambda_1^2 \sum_{n=0}^{m} \rho_n \psi_f' \cos^2\theta_n. \tag{21}$$

For the shear and extension tests, the integration and discretized analytical solutions, eqs. (18) and (21), are compared with a single-element numerical model. The integration and summation schemes agree and the FE results match exactly with the analytical solutions.

## 2.8. Finite element analysis of the DMV apparatus

*Geometry.* The mitral valve geometry is created by annotating the mitral annulus, papillary muscle tips and leaflet structure at end-diastole from the 3D echocardiography in the image computing platform 3D Slicer [44]. The echocardiographies are from two other patients diagnosed with the same phenotypes of DMV as in tissue modeling; FED and Barlow. The mitral annulus is generated by rotation around the geometric center of the annulus in the echocardiographic volume, cutting a plane every 30 degrees to evenly distribute the interpolation points that make up the annulus. The mitral valve leaflets are constructed by annotating the free edge and the leaflet structure at several echocardiographic planes, generating a point cloud describing the leaflets. Both the mitral annulus and the free edge are defined as NURBS curves, while the mitral leaflet surface is constructed using the leaflet points to guide a NURBS surface between the annulus and the free edge curve. The procedure for creating and annotating the geometry is illustrated in Fig. 7.

*Material parameters.* The material properties of the leaflets are described above. For the FED model, the material properties of A2, P2, and ALC are assigned to the anterior leaflet, posterior leaflet, and commissures, respectively, as shown in Fig. 8. In order to extend the quantified collagen distribution to the entire leaflets, a material orientation based on data from the study of Cochran et al. [45] is defined, see Fig. 6b in our previous study [13]. To avoid convergence problems, the neoHookean parameter is increased by 2 kPa for all samples. For the chordae, the material properties come from the study by Barber et al. [10]. A polynomial constitutive model is used with the five terms. The strain-energy function, say $\Psi_{chor}$, for the chordae is written as

$$\Psi_{chor} = \sum_{i=1}^{5} C_i (I_1 - 3)^i. \tag{22}$$

The non-zero constant for the marginal and strut chordae are $C_1 = 0.7694$, $C_5 = 26793$ and $C_1 = 0.05$, $C_5 = 772.8$, respectively. *Mesh* The mitral valve leaflets are modeled as shell elements due to the low thickness-to-area ratio. Three noded general-purpose shell elements with reduced integration (S3R) are used for the mitral valve leaflets. The FED leaflets mesh has 1 626 nodes and 3 021 elements,
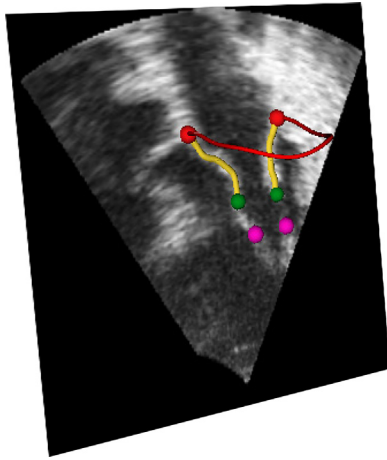
---

[3] <SMAASPUSERSUBROUTINES.HDR> is included in the subroutine to create global arrays and access during the analysis.

**Fig. 7.** Creating the geometry based on echocardiography and annotating annulus (red), leaflets (yellow), free edge (green), and papillary muscle tips (pink). (For interpretation of the references to colour in this figure legend, the reader is referred to the web version of this article.)
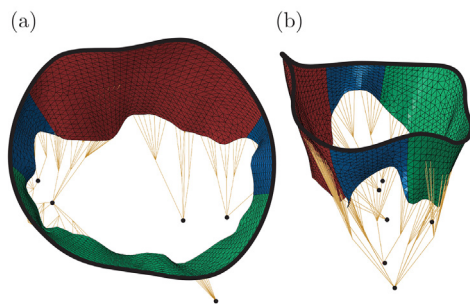


**Fig. 8.** FE model for the FED patient: (a) top (atrium) view and (b) side view; the material properties of the A2, P2, and ALC segments are assigned to the anterior leaflet (red), posterior leaflet (green) and commissures (blue), respectively. The annulus (black line) and papillary muscle tips (black dots) are imposed as displacement boundary conditions, while are annotated by echocardiography. Marginal and strut chordae (brown lines) connect the papillary muscle tips to the leaflets.. (For interpretation of the references to colour in this figure legend, the reader is referred to the web version of this article.)

while the significantly larger Barlow leaflets mesh has 4 356 nodes and 8 611 elements. Two-noded 3D truss elements (T3D2) are used for the chordae. The circular cross-sectional areas for myxomatous marginal and strut chordae are assumed to be 1.6 mm$^2$ and 2.2 mm$^2$, respectively. For the FED simulation, the prolapsing region was simulated by removing chordae along the free edge of the P2-P3 segment. First, a simulation was performed with physiologically marginal chordae around the free edge without any ruptured chordae. Then we observed a pathologic movement of a papillary muscle tip in the posteromedial commissure moving away from the annular plane during systole. This indicated that this papillary muscle was unloaded. By removing the marginal chordae attached to this papillary muscle, we were able to simulate a prolapse in a very good approximation to echocardiography.

*Boundary condition and loading.* In order to simulate the correct dynamics of the mitral valve, the annulus and papillary muscle tips are annotated in each time frame between end-diastole and peak systole. A pointwise mapping algorithm is then applied to each of these annular curves to minimize the total displacement between each consecutive curve as described in [46]. The annular and papillary muscle dynamics are then implemented as displacement boundary conditions using the Abaqus user subroutine VDISP. Marginal chordae were modeled to originate from each papillary

muscle (Fig. 8). Since the marginal chordae are difficult to distinguish on the echocardiography, they are each divided into several branches and inserted into the free edge of the leaflets [47]. For strut chordae, the insertion point on the leaflets is located using a 3D view of the left ventricle in EchoPAC (GE Healthcare, US). Similar to the marginal chordae, the strut chordae branch like a fan. The detailed method is described previously [13]. For a physiological disease-specific peak systolic pressure applied to the FE analyses, see Fig. 7 in our previous study [13]. Pressure was applied uniformly to the ventricular surface of the mitral valve leaflets. Peak systole pressure was set at 132 mmHg and 112 mmHg for the Barlow and FED patients, respectively.

*Validation.* To validate the numerical simulation, the leaflets are compared to the echocardiography at the peak systole. A point-to-mesh distance error is calculated by generating the peak systolic surface based on echocardiography and comparing it to the deformed mesh at the same time point [13].

## 3. Results

### 3.1. Mechanical properties and collagen microstructure of the DMV leaflets

Tissue clearing enables the full-depth SHG acquisition of DMV leaflets. SeeDBp clearing shows a minimal morphology alteration, as shown in Fig. 2. Shrinkage is limited to < 1% in the radial and circumferential directions. Additionally, utilizing forward and backward SHG signals improves the SNR in the thick Barlow sample. The collagen fiber emits more forward SHG signal, however, the forward signal suffers from low SNR in thick collagenous tissue due to the highly-scattering medium. On the other hand, the backward signal with sensitive detectors can enhance the SNR in layers closer to the objective where the forward signal is weakest. This concept is illustrated in Figs. 4 and 5. As shown in Fig. 5(c), the combined signal exhibits an enhanced SNR across the acquisition depth. Finally, due to the limited working distance of the objective, the image acquisition is performed on both sides. A high-accuracy motorized stage and using the markers as reference points ensured that the acquisition corresponded to the same spot on both sides.

The contour plots of Barlow and FED samples are shown in Fig. 9(a). The depth has been normalized for comparison. For Barlow and FED-P2 samples, it is clear that the collagen fiber distribution varies through the thickness. In addition, there is a mid-layer with little or no collagen fibers. In the case of Barlow, this collagen-free layer accounts for a considerable 40% of the thickness. The variation through the thickness of mean collagen fiber orientations and concentration parameters is shown in Table 1. The collagen-free layer can also be seen in Table 1. A representative plot is created for each contour plot as described in Section 2.4. The representative fiber distribution alongside the fitted von Mises distribution is shown in Fig. 9(b). The parameters of the fitted von Mises distribution are presented in Table 2. These parameters are used for the numerical simulation of the Barlow and FED mitral valve apparatus.

Quantified collagen fiber distribution from representative layer and planar biaxial mechanical tests is used to characterize the mechanical behavior of each sample. The experimental biaxial test data and the fitted model are shown in Fig. 9(c). The model is able to represent the mechanical behavior of the DMV leaflets. The estimated parameters of the model are presented in Table 3. The neoHookean parameter ($\mu$) has a low value ($\leq 1$kPa), which emphasizes the importance of the collagen fiber distribution to carry the load. These parameters are used in the numerical simulation of the DMV apparatus.
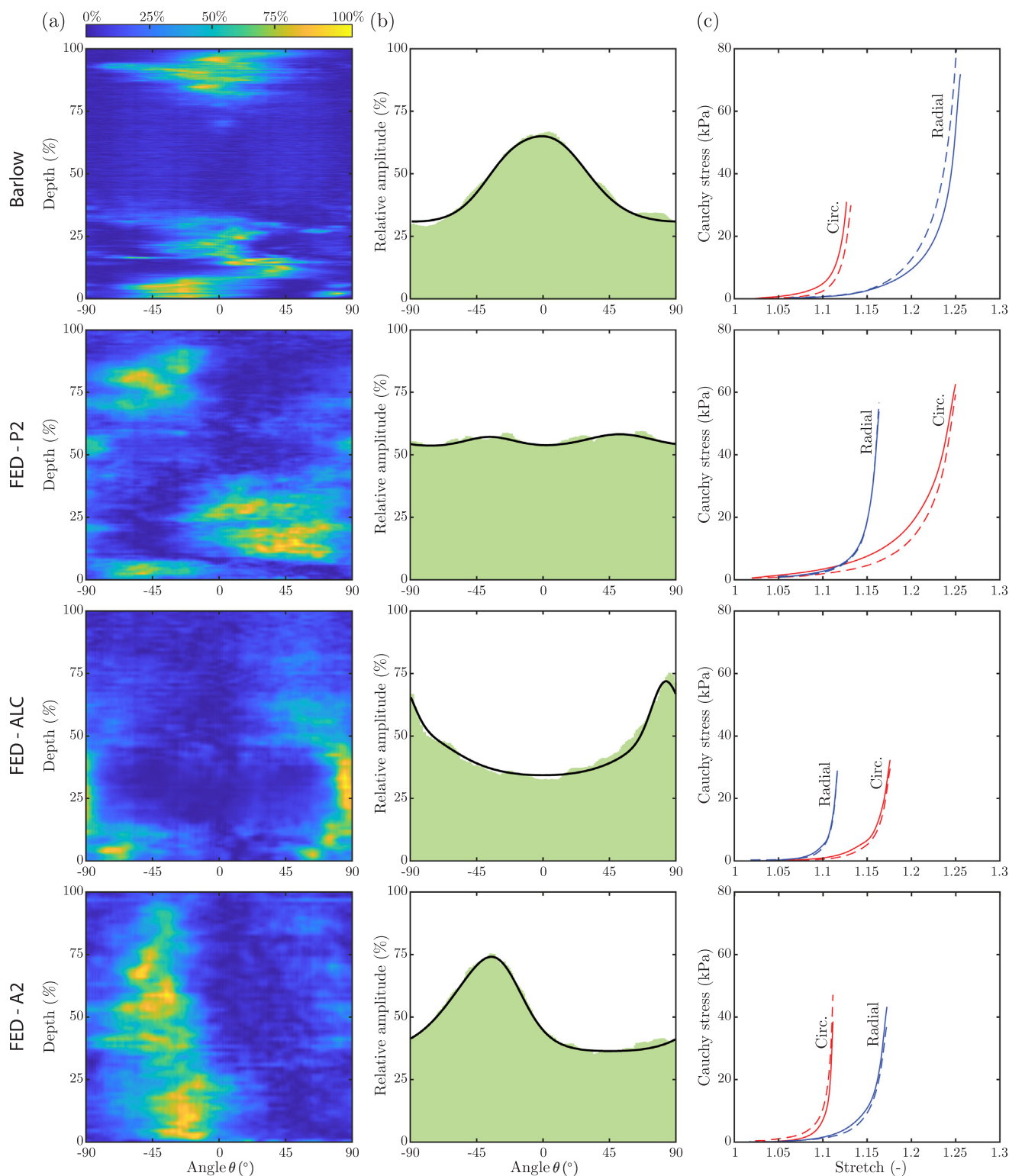
**Fig. 9.** Mechanical properties and collagen microstructure of DMV leaflets for Barlow and FED samples: (a) contour plots show the relative collagen amplitude based on depth and orientation; (b) representative collagen fiber distribution (green area) and fitted von Mises distribution (solid curve), note that the mean fiber orientation differs between samples.; (c) Cauchy stress versus stretch of the experimental data (dashed curve) and fitted constitutive model (solid curve) for radial (blue) and circumferential (red) directions. (For interpretation of the references to colour in this figure legend, the reader is referred to the web version of this article.)

## 3.2. Finite element analysis of the DMV apparatus

The numerical simulation is based on the quantified collagen microstructure (Table 2) and the characterized material properties (Table 3). The FE analysis is performed with discretization $m$ set to 180, i.e., every 1°. A higher discretization is possible, but the method resolution of the collagen fiber distribution is limited to 1°. The discretization scheme provides a computationally inexpensive approach to accurately account for fiber distribution and exclude fibers under compression. The total simulation time from

**Table 1**

Variation of mean fiber angles ($\alpha_1$, $\alpha_2$) and concentration parameters ($a_1$, $a_2$) through the thickness. The parameters are given for a 10% thickness interval. Depths without anisotropic layers are deliberately left out.

| Sample | Barlow | | | | FED-P2 | | | | FED-ALC | | | | FED-A2 | | | |
|---|---|---|---|---|---|---|---|---|---|---|---|---|---|---|---|---|
| Thickness | $\alpha_1(°)$ | $a_1(-)$ | $\alpha_2(°)$ | $a_2(-)$ | $\alpha_1(°)$ | $a_1(-)$ | $\alpha_2(°)$ | $a_2(-)$ | $\alpha_1(°)$ | $a_1(-)$ | $\alpha_2(°)$ | $a_2(-)$ | $\alpha_1(°)$ | $a_1(-)$ | $\alpha_2(°)$ | $a_2(-)$ |
| 0–10% | 8 | 6.34 | −29 | 4.36 | −24 | 2.08 | −55 | 2.65 | 88 | 15.93 | −76 | 0.93 | −22 | 8.84 | −23 | 4.13 |
| 10–20% | 30 | 8.89 | 7 | 5.69 | 60 | 5.65 | 24 | 2.67 | 82 | 11.28 | −80 | 0.8 | −21 | 4.64 | −52 | 4.47 |
| 20–30% | 15 | 10.9 | −12 | 3.47 | 60 | 1.75 | 8 | 2.16 | 88 | 18.81 | 83 | 1.05 | −18 | 1.92 | −64 | 4.24 |
| 30–40% | −2 | 3.83 | −52 | 2.48 | 63 | 1.6 | 13 | 3.02 | 86 | 17.75 | 71 | 0.8 | −13 | 2.82 | −47 | 3.45 |
| 40–50% | | | | | | | | | 84 | 9.76 | 57 | 0.47 | −30 | 6.68 | −57 | 3.33 |
| 50–60% | | | | | −68 | 0.61 | −87 | 8.64 | 65 | 2.34 | −67 | 3.64 | −43 | 5.56 | −52 | 1.5 |
| 60–70% | | | | | −40 | 6.71 | −81 | 4.27 | 70 | 1.34 | −85 | 2.37 | −55 | 2.26 | −68 | 2.52 |
| 70–80% | | | | | −49 | 4.69 | −66 | 1.17 | 58 | 1.47 | −63 | 1.53 | 87 | 3.3 | −59 | 2.55 |
| 80–90% | 8 | 2.76 | −16 | 5.17 | −35 | 11.62 | −57 | 1.69 | 50 | 3.48 | −49 | 3.63 | 80 | 1.46 | −44 | 6.16 |
| 90–100% | 17 | 2.1 | −20 | 3.68 | −24 | 8.26 | −45 | 1.4 | 45 | 4.87 | −23 | 4.83 | 69 | 3.03 | −41 | 2.7 |
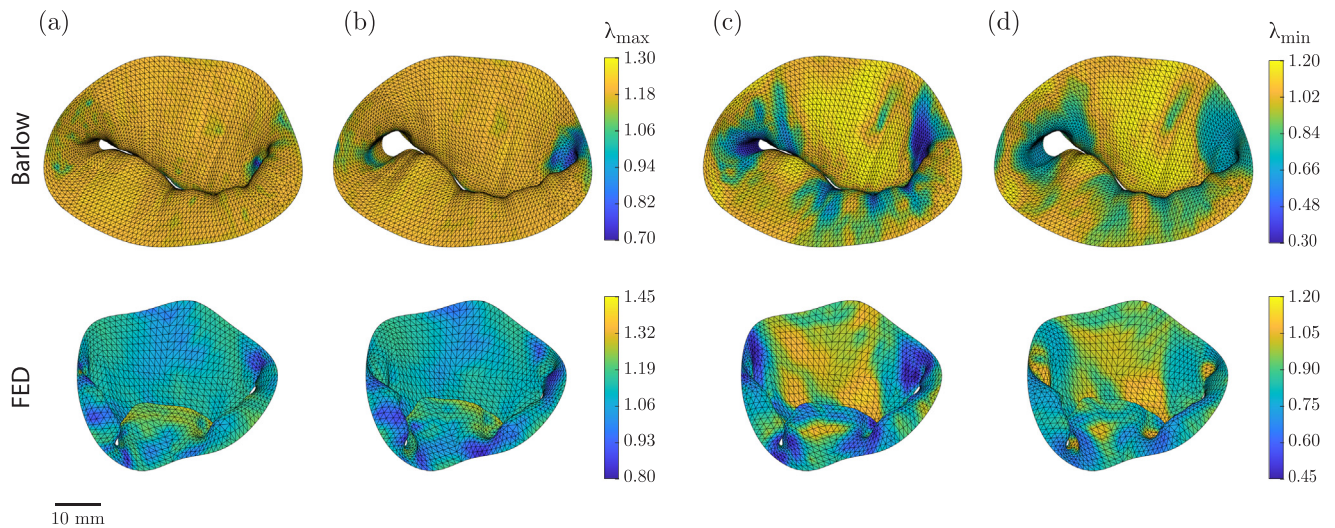


**Fig. 10.** Maximum and minimum principal stretches for Barlow and FED disease in peak systole: maximum principal stretch (a) with and (b) without exclusion of collagen fibers under compression. Minimum principal stretch (c) with and (d) without exclusion of collagen fibers under compression.

**Table 2**

Fitted von Mises parameters for representative collagen fiber distribution.

| Sample | $\alpha_1(°)$ | $a_1(-)$ | $\alpha_2(°)$ | $a_2(-)$ | $w(-)$ |
|---|---|---|---|---|---|
| Barlow | 8 | 1.34 | −25 | 2.45 | 0.76 |
| FED-P2 | 52 | 1.59 | −35 | 2.79 | 0.64 |
| FED-ALC | 83 | 10.18 | −90 | 0.96 | 0.21 |
| FED-A2 | −28 | 3.23 | −45 | 1.43 | 0.31 |

**Table 3**

Estimated mechanical properties and goodness-of-fit ($r^2$) based on planar biaxial tests and quantified collagen fiber distribution.

| Sample | $\mu$ (kPa) | $k_1$ (kPa) | $k_2(-)$ | $r^2$ |
|---|---|---|---|---|
| Barlow | 0.29 | 7.97 | 21.84 | 0.85 |
| FED-P2 | 1.08 | 17.08 | 9.55 | 0.92 |
| FED-ALC | 0.34 | 7.29 | 31.48 | 0.98 |
| FED-A2 | 0.38 | 3.38 | 47.33 | 0.97 |



**Fig. 11.** Percentage of fibers excluding compression for (a) Barlow and (b) FED FE analyses. 100% means all fibers are excluded.

end-diastole to peak systole was 53 and 44 minutes for the Barlow and the FED simulations, respectively. The simulation is performed on a workstation with an Intel Core i7-8700 CPU 3.20 GHz and MPI-parallelization with 8 logical processors in ABAQUS [32]. In addition, the same FE models are performed without excluding fibers under compression. The maximum and minimum principal stretches of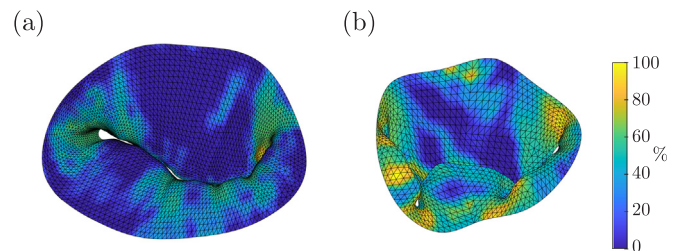 the Barlow and the FED numerical simulations in peak systole are shown in Fig. 10. The exclusion of compressed fibers allows for higher compression in folding regions, e.g., commissures, as shown in Fig. 10(c). Meanwhile, without exclusion, the model experiences significantly less compression.

Fig. 11 shows the percentage of collagen fiber exclusion for each element. A comparison of the Figs. 10 and 11 confirms that all fibers in the regions with negative maximum principal logarithmic strains are excluded, i.e., commissures. On the other hand, in regions with positive minimum principal logarithmic strains no fiber is excluded, i.e., belly regions. To validate the FE analysis, the mitral valve leaflets are compared to echocardiography at the peak systole. The point-to-mesh distance error map is shown in
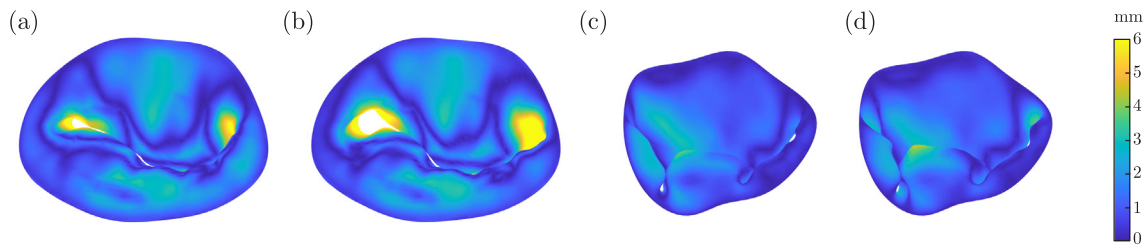
**Fig. 12.** Point-to-mesh distance error map at peak systole: Barlow simulation (a) with and (b) without excluding collagen fibers under compression. FED simulation (c) with and (d) without exclusion of collagen fibers under compression.
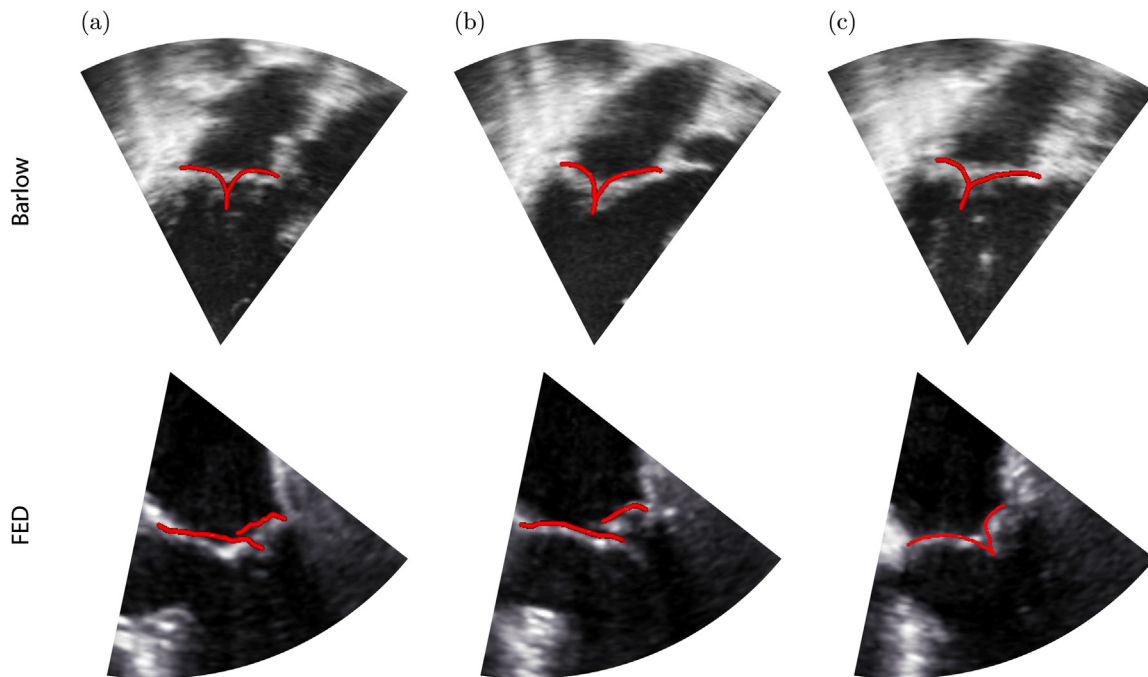


**Fig. 13.** Validation of FE model with echocardiography in (a) A1-P1, (b) A2-P2 and (c) A3-P3 planes for Barlow and FED model at peak systole.

Fig. 12. Again, the higher error in the commissure is observed in the case without the exclusion of compressed fibers. The average error value for the Barlow simulation is $2.02 \pm 1.8$ mm and $2.37 \pm 2.28$ mm, with and without fiber exclusion, respectively. For FED, this value is $1.05 \pm 0.79$ mm and $1.14 \pm 0.86$ mm, again with and without fiber exclusion, respectively.

The FE analyses are also compared to echocardiography at three acquisition planes, A1-P1, P2-A2, and A3-P3, as shown in Fig. 13. The numerical simulation captures the motion leaflets on all these planes with very good agreement. In addition, the prolapse in the A1-P1 and A2-P2 planes for the FED patient corresponds exactly to the echocardiography.

## 4. Discussion

DMV disease is the leading cause of primary mitral regurgitation. DMV is characterized by myxomatous degeneration that alters the microstructure of the mitral valve leaflets and, consequently, their mechanical properties. In this study, we characterized the mechanical properties and collagen dispersion of two phenotypes of DMV; FED with localized myxomatous degeneration and Barlow disease with diffused myxomatous degeneration. For FED, three samples from three anatomical segments are investigated, while

for Barlow's disease only one sample from the P2 segment is investigated.

The collagen dispersion of DMV leaflets is examined through the entire thickness using SHG microscopy. Tissue clearing is performed to enhance light transmission and facilitate in-depth imaging. SeeDB clearing is used for the Barlow sample, which preserves the geometry. For the thick Barlow sample, we also utilized the forward and backward SHG signal to increase the signal-to-noise ratio. As shown in Fig. 5, the backward SHG with highly-sensitive HyD detectors provided better SNR in the first $300\,\mu$m while the forward SHG provided better SNR at greater depth.

The contour plot of collagen fiber distribution shows a collagen-free layer in the Barlow and FED-P2 samples. This finding can be attributed to the expansion of the spongiosa layer, a feature of myxomatous degeneration. This collagen-free layer in the Barlow sample occupies a thickness of 40%, which is in agreement with previous histological analyses [5–7]. Furthermore, it is observed in the FED-P2 sample that this collagen-free layer is thinner than in the Barlow sample, which also agrees with the literature [6,7]. The FED-ALC and FED-A2 samples exhibit a collagen distribution resemble healthy tissue whose histological analysis shows a thick layer of fibrosa [5–7]. They also have a consistent mean fiber orientation throughout the thickness, as can be seen from Fig. 9(a)

and Table 1. FED-P2 and Barlow samples, on the other hand, have variable mean fiber orientation through the thickness. The regional difference in FED samples can be related to the localized myxomatous degeneration in FED. In fact, the posterior leaflets, in particular P2 segments, are usually the most commonly affected segment in FED [7], as observed in this study.

A representative fiber distribution layer is defined for mechanical property estimation and numerical simulation, see Fig. 9(b). Barlow and FED-P2 samples showed a lower concentration parameter, i.e., a higher dispersion value. We hypothesize that this is due to myxomatous degeneration, often associated with increased growth and fragmentation of collagen fibers. As already mentioned, the FED-A2 and FED-ALC samples are probably less affected by myxomatous degeneration, which explains the higher concentration parameter. Nevertheless, all samples show an anisotropic collagen fiber distribution.

Planar biaxial tests also revealed anisotropic mechanical behavior of the tissue, shown in Fig. 9(c). Even the Barlow sample with diffuse myxomatous degeneration behaves anisotropically. This is in contrast to uniaxial tests of myxomatous MV leaflets in the study of Barber et al. [10]. Also, contrary to what is commonly assumed for mitral valve leaflets, the circumferential direction is not necessarily the stiffer direction. In fact, previous studies have shown that collagen orientation is circumferential in the belly of the anterior leaflets and radial in the commissures [22,45]. Nonetheless, the stiffer direction is consistent with the quantified collagen fiber distribution. For the FED-P2 sample, with two distinct families of fibers oriented at $52°$ and $-35°$ with respect to the circumferential direction, a stronger anisotropy than expected is observed. This finding may account for the contribution to the mechanical behavior of other matrix components, e.g., elastin.

Again, the Barlow and FED-P2 samples show higher extensibility, possibly due to collagen fragmentation in myxomatous degeneration. In addition, the extensibility for all samples is lower than the reported value $(37 - 39\%)$ based on uniaxial tests [10]. A very low neoHookean parameter is estimated for all samples. A previous study [13] used the inverse FE model and the uniaxial data from Barber et al. [10] to characterize the material behavior based on the model [48]. The estimated neoHookean parameter was 1 kPa, comparable to our finding in this study. The low neoHookean parameter underlines the importance of collagen fibers and their distribution for the mechanical properties of MV leaflets and thus for the function of the MV apparatus.

We also implemented a constitutive model that can exclude collagen fibers under compression. Collagen fibers are wavy and therefore cannot withstand compressive load, as commonly assumed in soft tissue modeling [42,48]. This is particularly important in the case of the mitral valve apparatus, since the leaflet material should behave softer in the commissure to facilitate folding, while in the belly it should be stiff enough to prevent bulging. We used the previously developed pipeline to create a patient-specific FE model from a FED and a Barlow patient. The numerical simulation results showed an improved point-to-mesh distance error compared to the previous studies [13,17], especially in the belly region. If we use the same model without fiber exclusion, the errors in the commissure and folding regions, i.e., P1-P2 and P2-P3, are higher. It can be concluded that the properties of the collagen fibers found in this study are stiffer than our previous study [13], based on uniaxial tests from Barber et al. [10]. This results in less bulging in the belly region (Fig. 13), however, collagen fibers under compression should be excluded to allow MV closure, as shown in Figs. 10 and 12.

There are several limitations to the current study. First is the limited number of samples examined in this study. However, the difficulty in obtaining and testing samples limits further examination. In recent years, the combination of multiple surgical techniques has reduced the need for resections of large tissues amenable to mechanical biaxial testing. Indeed. For the first time, we study the collagen microstructure and mechanical behavior of DMV leaflets using planar biaxial tests. Although further studies are needed for a unanimous conclusion, this study provides insight into how DMV and its phenotypes alter the collagen microstructure and thus the mechanics of the MV apparatus. Also, we only had access to the P2 segment of Barlow's disease. In the surgical procedure, posterior leaflets, especially the P2 segment, are the most commonly resected segment, while the anterior leaflet is rarely resected. Therefore, we hypothesized that the mechanical properties of the entire leaflet are similar in Barlow's disease, as it is described as diffuse myxomatous degeneration. Second, although tissue modeling based on the representative layer was able to capture the mechanical behavior of DMV leaflets, see Fig. 9 and $r^2$ in Table 3, more accurate modeling can be performed in the future. The detailed through-the-thickness collagen structure quantified in this study can be used for a multi-layer model. This detailed layer-by-layer information is not available in other studies based on polarized spatial frequency domain imaging [26,27] and small-angle X-ray or light scattering [29–31]. The multi-layer model will have the potential to accurately assess the cellular mechanical response to valve interstitial cells, which have been shown to be the major contributor to DMV disease, see, e.g., the study by Levine et al. [5]. Furthermore, the multi-layer model will improve the modeling, especially in the case of different mean fiber orientations across the thickness, as shown by the lower goodness-of-fit value for Barlow and FED-P2. Third, the echocardiography we used for the FE model is not from the same patients in which we studied the mechanical properties and collagen microstructure. The reason is that neither FED nor the Barlow patient from whom the tissue is resected, had 3D echocardiography. In fact, the FED patient had undergone acute surgery. Nevertheless, the numerical simulations are being improved taking into account the disease-specific mechanical properties and more realistic constitutive models. Previously, we showed that in silico analysis provides insights for patient-specific annuloplasty in Barlow disease [49]. An accurate disease-specific material model like the one presented in this study would improve the accuracy of such in silico studies. Fourth, the chordae in the model were split in a fan-like fashion by then inserting them into the free edge or belly of the leaflet. This leads to a high-stress concentration at the insertion points. Anatomically, the leaflet is thicker at the chordae insertion point because the chordae smoothly transition into leaflets. More accurate chordae modeling would provide valuable and reliable information for stress analysis between FED and Barlow. Finally, the lack of healthy human samples limits the conclusion of the current study. The comparison with healthy tissue will enable the following questions to be answered: how does myxomatous degeneration affect collagen dispersion and mechanical properties? Are the A2 and ALC samples from FED patients similar to healthy tissue in terms of collagen dispersion and mechanical properties? How would the mitral valve apparatus function if we assumed a healthy tissue model for the FED and the Barlow's mitral valve?

## 5. Conclusions

In this study, we investigated the mechanical behavior of Barlow and fibroelastic deficiency tissues. We also examined the collagen orientations of the sample throughout the thickness. The information is used for a constitutive model that can exclude collagen fibers under compression. The FE model showed accurate prediction compared to echocardiography. Compared to the previous model, which used a simplified model based on uniaxial test data, the current study improved the point-to-mesh distance error. The versatility of the material model, which is stiff in the belly and

very soft in the commissures, resulted in better agreement with echocardiography.

## Declaration of Competing Interest

The authors declare that they have no known competing financial interests or personal relationships that could have appeared to influence the work reported in this paper.

## References

[1] B. Iung, V. Delgado, R. Rosenhek, S. Price, B. Prendergast, O. Wendler, M. De Bonis, C. Tribouilloy, A. Evangelista, A. Bogachev-Prokophiev, A. Apor, H. Ince, C. Laroche, B.A. Popescu, L. Piérard, M. Haude, G. Hindricks, F. Ruschitzka, S. Windecker, J.J. Bax, A. Maggioni, A. Vahanian, A. Goda, J. Mascherbauer, F. Samadov, A. Pasquet, K. Linhartova, N. Ihlemann, M. Abdelhamid, A. Saraste, C. Tribouilloy, E.S. Kostovska, G. Bajraktari, E. Mirrakhimov, A. Erglis, V. Mizariene, D. Cassar, V. Delgado, L. Tomkiewicz-Pajak, R. Ribeiras, B. Beleslin, I. Simkova, A. Evangelista, S.M. Dogan, S. Rahman-Haley, Contemporary presentation and management of valvular heart disease, Circulation 140 (14) (2019) 1156–1169, doi:10.1161/CIRCULATIONAHA.119.041080.

[2] V.T. Nkomo, J.M. Gardin, T.N. Skelton, J.S. Gottdiener, C.G. Scott, M. Enriquez-Sarano, Burden of valvular heart diseases: a population-based study, The Lancet 368 (9540) (2006) 1005–1011, doi:10.1016/S0140-6736(06)69208-8.

[3] D.H. Adams, R. Rosenhek, V. Falk, Degenerative mitral valve regurgitation: best practice revolution, Eur. Heart J. 31 (16) (2010) 1958–1966, doi:10.1093/eurheartj/ehq222.

[4] C. Antoine, F. Mantovani, G. Benfari, S.V. Mankad, J.F. Maalouf, H.I. Michelena, M. Enriquez-Sarano, Pathophysiology of degenerative mitral regurgitation, Circulation: Cardiovascular Imaging 11 (1) (2018) e005971, doi:10.1161/CIRCIMAGING.116.005971.

[5] R.A. Levine, A.A. Hagége, D.P. Judge, M. Padala, J.P. Dal-Bianco, E. Aikawa, J. Beaudoin, J. Bischoff, N. Bouatia-Naji, P. Bruneval, J.T. Butcher, A. Carpentier, M. Chaput, A.H. Chester, C. Clusel, F.N. Delling, H.C. Dietz, C. Dina, R. Durst, L. Fernandez-Friera, M.D. Handschumacher, M.O. Jensen, X.P. Jeunemaitre, H.L. Marec, T.L. Tourneau, R.R. Markwald, J. Mérot, E. Messas, D.P. Milan, T. Neri, R.A. Norris, D. Peal, M. Perrocheau, V. Probst, M. Pucéat, N. Rosenthal, J. Solis, J.-J. Schott, E. Schwammenthal, S.A. Slaugenhaupt, J.-K. Song, M.H. Yacoub, Mitral valve diseasemorphology and mechanisms, Nat. Rev. Cardiol. 12 (2015) 689–710, doi:10.1038/nrcardio.2015.161.

[6] J. Hjortnaes, J. Keegan, P. Bruneval, E. Schwartz, F.J. Schoen, A. Carpentier, R.A. Levine, A. Hagège, E. Aikawa, Comparative histopathological analysis of mitral valves in Barlow disease and fibroelastic deficiency, Semin. Thorac. Cardiovasc. Surg. 28 (4) (2016) 757–767, doi:10.1053/J.SEMTCVS.2016.08.015.

[7] A.L. van Wijngaarden, B.P.T. Kruithof, T. Vinella, D.Q.C.M. Barge-Schaapveld, N. Ajmone Marsan, Characterization of degenerative mitral valve disease: differences between fibroelastic deficiency and barlows disease, J. Cardiovasc. Dev. Dis. 8 (2) (2021) 23, doi:10.3390/jcdd8020023.

[8] M.A. Clavel, F. Mantovani, J. Malouf, H.I. Michelena, O. Vatury, M.S. Jain, S.V. Mankad, R.M. Suri, M. Enriquez-Sarano, Dynamic phenotypes of degenerative myxomatous mitral valve disease, Circulation: Cardiovascular Imaging 8 (5) (2015) e002989, doi:10.1161/CIRCIMAGING.114.002989/FORMAT/EPUB.

[9] W.A. Zoghbi, D. Adams, R.O. Bonow, M. Enriquez-Sarano, E. Foster, P.A. Grayburn, R.T. Hahn, Y. Han, J. Hung, R.M. Lang, S.H. Little, D.J. Shah, S. Shernan, P. Thavendiranathan, J.D. Thomas, N.J. Weissman, Recommendations for noninvasive evaluation of native valvular regurgitation, J. Am. Soc. Echocardiogr. 30 (4) (2017) 303–371, doi:10.1016/j.echo.2017.01.007.

[10] J.E. Barber, F.K. Kasper, N.B. Ratliff, D.M. Cosgrove, B.P. Griffin, I. Vesely, Mechanical properties of myxomatous mitral valves, J. Thorac. Cardiovasc. Surg. 122 (5) (2001) 955–962, doi:10.1067/mtc.2001.117621.

[11] F. Dal Pan, G. Donzella, C. Fucci, M. Schreiber, Structural effects of an innovative surgical technique to repair heart valve defects, J. Biomech. 38 (12) (2005) 2460–2471, doi:10.1016/J.JBIOMECH.2004.10.005.

[12] Q. Zhong, W. Zeng, X. Huang, M. Su, Y. Luo, Constitutive modeling and finite element analysis of myxomatous mitral leaflet tissue, J. Mech. Med. Biol. 14 (03) (2014) 1450031, doi:10.1142/S0219519414500316.

[13] H.M. Aguilera, S. Urheim, B. Skallerud, V. Prot, Influence of annular dynamics and material behavior in finite element analysis of Barlows mitral valve disease, J. Elast. 145 (1–2) (2021) 163–190, doi:10.1007/s10659-021-09829-5.

[14] H.M. Aguilera, S. Urheim, R.M. Persson, R. Haaverstad, B. Skallerud, V. Prot, Finite element analysis of mitral valve annuloplasty in Barlows disease, J. Biomech. 142 (2022) 111226, doi:10.1016/J.JBIOMECH.2022.111226.

[15] E. Votta, F. Maisano, S.F. Bolling, O. Alfieri, F.M. Montevecchi, A. Redaelli, The geoform disease-specific annuloplasty system: afinite element study, Ann. Thorac. Surg. 84 (1) (2007) 92–101, doi:10.1016/J.ATHORACSUR.2007.03.040.

[16] Q. Wang, W. Sun, Finite element modeling of mitral valve dynamic deformation using patient-specific multi-slices computed tomography scans, Ann. Biomed. Eng. 41 (1) (2013) 142–153, doi:10.1007/s10439-012-0620-6.

[17] T. Pham, C. Martin, J. Elefteriades, C. Primiano, F. Kong, W. Sun, Q. Wang, R. McKay, Finite element analysis of patient-specific mitral valve with mitral regurgitation, Cardiovasc. Eng. Technol. 8 (1) (2017) 3–16, doi:10.1007/s13239-016-0291-9.

[18] A. Choi, D.D. McPherson, H. Kim, Computational virtual evaluation of the effect of annuloplasty ring shape, Int. J. Numer. Method. Biomed. Eng. 33 (6) (2017) e2831, doi:10.1002/CNM.2831.

[19] F. Kong, A. Caballero, R. McKay, W. Sun, Finite element analysis of MitraClip procedure on a patient-specific model with functional mitral regurgitation, J. Biomech. 104 (2020) 109730, doi:10.1016/j.jbiomech.2020.109730.

[20] V. Prot, B. Skallerud, G. Sommer, G. Holzapfel, On modelling and analysis of healthy and pathological human mitral valves: two case studies, J. Mech. Behav. Biomed. Mater. 3 (2) (2010) 167–177, doi:10.1016/j.jmbbm.2009.05.004.

[21] P. Vandemaele, K. Vander Linden, S. Deferm, R. Jashari, F. Rega, P. Bertrand, P. Vandervoort, J. Vander Sloten, N. Famaey, H. Fehervary, Alterations in human mitral valve mechanical properties secondary to left ventricular remodeling: a biaxial mechanical study, Front. cardiovasc. med. 9 (June) (2022) 1–16, doi:10.3389/fcvm.2022.876006.

[22] M.J. Sadeghinia, B. Skallerud, G.A. Holzapfel, V. Prot, Biomechanics of mitral valve leaflets: second harmonic generation microscopy, biaxial mechanical tests and tissue modeling, Acta. Biomater. 141 (2022) 244–254, doi:10.1016/j.actbio.2022.01.003.

[23] K. May-Newman, F.C.-P. Yin, A constitutive law for mitral valve tissue, J. Biomech. Eng. 120 (1) (1998) 38, doi:10.1115/1.2834305.

[24] V. Prot, B. Skallerud, G.A. Holzapfel, Transversely isotropic membrane shells with application to mitral valve mechanics. constitutive modelling and finite element implementation, Int. J. Numer. Methods. Eng. 71 (8) (2007) 987–1008, doi:10.1002/nme.1983.

[25] W. Zhang, S. Ayoub, J. Liao, M.S. Sacks, A meso-scale layer-specific structural constitutive model of the mitral heart valve leaflets, Acta. Biomater. 32 (2016) 238–255, doi:10.1016/j.actbio.2015.12.001.

[26] S.V. Jett, L.T. Hudson, R. Baumwart, B.N. Bohnstedt, A. Mir, H.M. Burkhart, G.A. Holzapfel, Y. Wu, C.H. Lee, Integration of polarized spatial frequency domain imaging (pSFDI) with a biaxial mechanical testing system for quantification of load-dependent collagen architecture in soft collagenous tissues, Acta. Biomater. 102 (2020) 149–168, doi:10.1016/j.actbio.2019.11.028.

[27] D.J. Fitzpatrick, K. Pham, C.J. Ross, L.T. Hudson, D.W. Laurence, Y. Yu, C.-H. Lee, Ex vivo experimental characterizations for understanding the interrelationship between tissue mechanics and collagen microstructure of porcine mitral valve leaflets, J. Mech. Behav. Biomed. Mater. 134 (2022) 105401, doi:10.1016/J.JMBBM.2022.105401.

[28] S. Ayoub, K.C. Tsai, A.H. Khalighi, M.S. Sacks, The three-dimensional microenvironment of the mitral valve: insights into the effects of physiological loads, Cell. Mol. Bioeng. 11 (4) (2018) 291–306, doi:10.1007/S12195-018-0529-8/FIGURES/11.

[29] M.S. Sacks, D.B. Smith, E.D. Hiester, The aortic valve microstructure: effects of transvalvular pressure, J. Biomed. Mater. Res. 41 (1) (1998) 131141, doi:10.1002/(SICI)1097-4636(199807)41:1⟨131::AID-JBM16⟩3.0.CO;2-Q.

[30] J. Liao, L. Yang, J.S. Grashow, M.S. Sacks, The relation between collagen fibril kinematics and mechanical properties in the mitral valve anterior leaflet, J. Biomech. Eng. 129 (1) (2007) 78–87, doi:10.1115/1.2401186.

[31] A.D. Pant, V.S. Thomas, A.L. Black, T. Verba, J.G. Lesicko, R. Amini, Pressure-induced microstructural changes in porcine tricuspid valve leaflets, Acta. Biomater. 67 (2018) 248–258, doi:10.1016/j.actbio.2017.11.040.

[32] Abaqus: Dassault Systèmes Simulia Corp., Providence, RI, USA, 2019. www.simulia.com.

[33] S.D. Salinas, M.M. Clark, R. Amini, The effects of -80°c short-term storage on the mechanical response of tricuspid valve leaflets, J Biomech 98 (2020) 109462, doi:10.1016/j.jbiomech.2019.109462.

[34] V. Ayyalasomayajula, B. Skallerud, Microstructure and mechanics of the bovine trachea: layer specific investigations through SHG imaging and biaxial testing, J. Mech. Behav. Biomed. Mater. 134 (2022) 105371, doi:10.1016/j.jmbbm.2022.105371.

[35] J.A. Dent, A.G. Polson, M.W. Klymkowsky, A whole-mount immunocytochemical analysis of the expression of the intermediate protein vimentin in xenopus, Development 105 (1989) 61–74, doi:10.1242/dev.105.1.61.

[36] M.-T. Ke, S. Fujimoto, T. Imai, SeeDB: a simple and morphology-preserving optical clearing agent for neuronal circuit reconstruction, Nat. Neurosci. 16 (8) (2013) 1154–1161, doi:10.1038/nn.3447.

[37] D.S. Richardson, J.W. Lichtman, Clarifying tissue clearing, Cell 162 (2) (2015) 246–257, doi:10.1016/j.cell.2015.06.067.

[38] A.J. Schriefl, H. Wolinski, P. Regitnig, S.D. Kohlwein, G.A. Holzapfel, An automated approach for three-dimensional quantification of fibrillar structures in optically cleared soft biological tissues, J. R. Soc. Interface. 10 (80) (2012) 20120760, doi:10.1098/rsif.2012.0760.

[39] F. Légaré, C. Pfeffer, B.R. Olsen, The role of backscattering in SHG tissue imaging, Biophys. J. 93 (4) (2007) 1312–1320, doi:10.1529/BIOPHYSJ.106.100586.

[40] S. Federico, W. Herzog, Towards an analytical model of soft biological tissues, J. Biomech. 41 (16) (2008) 3309–3313, doi:10.1016/J.JBIOMECH.2008.05.039.

[41] K. Li, R.W. Ogden, G.A. Holzapfel, A discrete fibre dispersion method for excluding fibres under compression in the modelling of fibrous tissues, J. R. Soc. Interface 15 (138) (2018) 20170766, doi:10.1098/rsif.2017.0766.

[42] G.A. Holzapfel, T.C. Gasser, R.W. Ogden, A new constitutive framework for arterial wall mechanics and a comparative study of material models, J. Elast. 61 (1–3) (2000) 1–48, doi:10.1023/A:1010835316564.

[43] G.A. Holzapfel, Nonlinear solid Mechanics. A Continuum Approach for Engineering, John Wiley & Sons, Chichester, 2000.

[44] R. Kikinis, S.D. Pieper, K.G. Vosburgh, 3D slicer: a platform for subject-specific image analysis, visualization, and clinical support, in: F.A. Jolesz (Ed.), Intraoperative Imaging and Image-Guided Therapy, Springer New York, New York, NY, 2014, pp. 277–289, doi:10.1016/j.mri.2012.05.001.

[45] R.P. Cochran, K.S. Kunzelman, C.J. Chuong, M.S. Sacks, R.C. Eberhart, Nondestructive analysis of mitral valve collagen fiber orientation, ASAIO transactions 37 (3) (1991) 447–448. http://www.ncbi.nlm.nih.gov/pubmed/1751231.

[46] B.V. Rego, A.H. Khalighi, A. Drach, E.K. Lai, A.M. Pouch, R.C. Gorman, J.H. Gorman, M.S. Sacks, A noninvasive method for the determination of in vivo mitral valve leaflet strains, Int. J. Numer. Method. Biomed. Eng. 34 (12) (2018) e3142, doi:10.1002/cnm.3142.

[47] K.S. Kunzelman, R.P. Cochran, E.D. Verrier, R.C. Eberhart, Anatomic basis for mitral valve modelling, J. Heart Valve Dis. 3 5 (1994) 491–496.

[48] T.C. Gasser, R.W. Ogden, G.A. Holzapfel, Hyperelastic modelling of arterial layers with distributed collagen fibre orientations, J. R. Soc. Interface 3 (6) (2006) 15–35, doi:10.1098/rsif.2005.0073.

[49] H.M. Aguilera, R.M. Persson, R. Haaverstad, B. Skallerud, V. Prot, S. Urheim, In silico analysis provides insights for patient-specific annuloplasty in barlow disease, JTCVS Open (2023), doi:10.1016/j.xjon.2023.01.007.